

---

# INFERRING LARGE-SCALE STRUCTURAL CONNECTIVITY FROM LOCAL ACTIVITY IN A MODEL OF THE MOUSE LARGE-SCALE CORTICAL NETWORK

---

Ronaldo V. Nunes<sup>1</sup>, Marcelo Bussotti Reyes<sup>1</sup>, Jorge F. Mejias<sup>2</sup>, and Raphael Y. de Camargo<sup>1</sup>

<sup>1</sup>Center for Mathematics, Computing and Cognition, Universidade Federal do ABC, São Bernardo  
do Campo, Brazil

<sup>2</sup>Swammerdam Institute for Life Sciences, University of Amsterdam, Amsterdam, The Netherlands

January 28, 2021

## ABSTRACT

1        Inferring the structural connectivity from electrophysiological measurements is a  
2        fundamental challenge in systems neuroscience. Directed functional connectivity  
3        measures, such as the Generalized Partial Directed Correlation (GPDC), provide  
4        estimates of the causal influence between areas. However, such methods have a limi-  
5        tation because their estimates depend on the number of brain regions simultaneously  
6        recorded. We analyzed this problem by evaluating the effectiveness of GPDC to  
7        estimate the connectivity of a ground-truth, data-constrained computational model of  
8        a large-scale mouse cortical network. The model contains 19 cortical areas modeled  
9        using spiking neural populations, and directed weights for long-range projections  
10        were obtained from a tract-tracing cortical connectome. We show that the GPDC  
11        estimates correlate positively with structural connectivity. Moreover, the correlation

12 between structural and directed functional connectivity is comparable even when  
13 using only a few cortical areas for GPDC estimation, a typical scenario for electro-  
14 physiological recordings. Finally, GPDC measures also provided a measure of the  
15 flow of information among cortical areas.

## 16 **1 Introduction**

17 The communication between brain regions is often analyzed through structural and functional  
18 connectivity [1]. The former refers to anatomical connections between brain regions generally  
19 quantified using tracer injections or diffusion magnetic resonance imaging [2]. The map of these  
20 connections is called “connectome” [3], whose analysis includes methods to evaluate the networks  
21 defined by nodes (brain regions) and edges (synapses) [4, 5]. Functional connectivity evaluates  
22 brain communication from statistical relations between recorded brain signals [6, 1]. Particularly,  
23 directed functional connectivity methods use the concept of causality to infer both the intensity and  
24 the direction of the connections between brain regions [7]. Even though there is some association  
25 between structural and functional connectivity, the relationship between them is not straightfor-  
26 ward [1]. While the former is practically static and compose the map of possible pathways for  
27 information flow between brain regions, the latter changes continuously and depends, for example,  
28 on the dynamical states of brain regions, noise, and strength of structural connections [8].

29 During electrophysiological procedures, researchers typically record brain signals using electrodes  
30 positioned in different depths of brain regions. Even with the improvement in technologies for  
31 recording signals, it is usually possible to record signals only from a few areas compared to the  
32 number of sources of activity in the brain [9, 10, 11]. Thus, the functional connectivity analysis  
33 presents a problem because many regions that may perform as common inputs [7], and influence  
34 indirectly other regions [12, 6] are not recorded. Therefore, the comparison between structural  
35 and functional connectivity is problematic since spurious inferred causality relations can lead to  
36 misinterpretations of electrophysiological data.

37 Some simulation studies evaluated the relation between directed functional connectivity and struc-  
38 tural connections [8, 13, 14, 15]. However, most of these studies used either autoregressive models  
39 for the dynamics of each node [16] or rate-based models [13]. These studies provided impor-  
40 tant steps towards evaluating the reliability of causality measures, but they are still distant from  
41 laboratory experimental conditions.

42 In this work, we investigated the relationship between directed functional connectivity and structural  
43 connectivity in a large-scale spiking neuronal network model of the cortex, derived from a cortical  
44 connectome of the mouse obtained using tracer injections [17]. Causality measures obtained using  
45 GPDC explained most of the variance of structural connection strengths. The mean correlation  
46 remained high ( $r > 0.6$ ) even when only a few cortical areas were considered in the GPDC  
47 calculation, indicating that this causality measure provides reliable results in typical experimental  
48 conditions in which only recordings from a subset of areas are available.

## 49 **2 Methods**

### 50 **2.1 Neuron model**

51 We modeled the neurons using a single-compartment Hodgkin–Huxley-type model, where the  
52 membrane potential of the  $i$ -th neuron described by,

$$C_m \frac{dV_i}{dt} = -g_{Na} m_i^3 h_i (V - E_{Na}) - g_K n_i^4 (V - E_K) - g_L (V - E_L) + I_{ext,i} + I_{syn,i}, \quad (1)$$

53 the membrane capacitance  $C_m$  is 0.50 nF (0.125 nF) for excitatory (inhibitory) neurons. The  
54 maximal conductances values were  $g_{Na} = 12.5 \mu\text{S}$ ,  $g_K = 4.74 \mu\text{S}$  and  $g_L = 0.025 \mu\text{S}$ . The  
55 reversal potentials  $E_{Na} = 40 \text{ mV}$ ,  $E_K = -80 \text{ mV}$ , and  $E_L = -65 \text{ mV}$  correspond to the sodium,  
56 potassium and leakage channel, respectively [18]. The dynamics of the voltage-gated ion channels  
57 are described by activation and inactivation variables  $m$ ,  $n$ , and  $h$ , where  $m$  and  $n$  accounts for the

58 dynamics of Na channels and  $h$  for K channels. The probability that an ion channel is open evolves  
59 according to a set of ordinary differential equations [19],

$$\frac{dm}{dt} = \alpha_m(V)(1 - m) - \beta_m(V)m, \quad (2)$$

$$\frac{dh}{dt} = \alpha_h(V)(1 - h) - \beta_h(V)h, \quad (3)$$

$$\frac{dn}{dt} = \alpha_n(V)(1 - n) - \beta_n(V)n, \quad (4)$$

60 where,

$$\alpha_m(V) = 0.1 \frac{(V+16)}{1 - \exp(-(V+16)/10)}, \quad (5)$$

$$\beta_m(V) = 4 \exp(-(V + 41)/18), \quad (6)$$

$$\alpha_h(V) = 0.07 \exp(-(V + 30)/20), \quad (7)$$

$$\beta_h(V) = [1 + \exp(-V/10)]^{-1}, \quad (8)$$

$$\alpha_n(V) = 0.01 \frac{(V+20)}{1 - \exp(-(V+20)/10)}, \quad (9)$$

$$\beta_n(V) = 0.125 \exp(-(V + 30)/80), \quad (10)$$

61 The parameters used in this neuron model was previously reported and applied in some studies that  
62 modeled cortical neuronal populations. [20, 19, 21]

## 63 2.2 Spiking neuronal population model

64 Each spiking neuronal population was composed of 2000 neurons, 1600 excitatory and 400 in-  
65 hibitory. Neurons within each spiking neuronal population were randomly connected with proba-  
66 bility  $p_{\text{intra}} = 10\%$ . The synaptic current  $I_{\text{syn}}$  that arrives to postsynaptic neuron  $i$  is modeled by,

67

$$I_{\text{syn},i}(t) = \sum_{j \in \text{presyn}} g_{\text{syn},i,j}(t) [E_{\text{syn}} - V_i(t)], \quad (11)$$

68 where the index  $j$  represent a presynaptic neuron connected to neuron  $i$  and the sum over  $j$  accounts  
 69 for all the synapses that impinge on neuron  $i$ .  $E_{\text{syn}}$  is the synaptic reversal potential which is 0 mV  
 70 for excitatory and  $-70$  mV for inhibitory synapses. The dynamics of synaptic conductance  $g_{\text{syn},i,j}$   
 71 is described by an exponential function as follows [22],

$$\frac{dg_{\text{syn},i,j}}{dt} = -\frac{g_{\text{syn},i,j}}{\tau}. \quad (12)$$

72 When a presynaptic neuron  $j$  fires a spike, a synaptic weight  $w$  is added on the synaptic conductance  
 73  $g_{\text{syn},i,j}$  after the axonal delay, which was set as 1 ms [19]. The value of  $w$  depends on the excita-  
 74 tory/inhibitory nature of the presynaptic and postsynaptic neurons. The synaptic time constant  $\tau$  is  
 75 2 ms and 8 ms for excitatory and inhibitory synapses, respectively. Furthermore, all neurons receive  
 76 a background input given by a heterogeneous Poisson-process spiking activity with a rate of 7.3  
 77 kHz [19]. The effect of the background input in each neuron is an excitatory synaptic current. To  
 78 add heterogeneity in our model, all synaptic weights  $w$  for recurrent connections and background  
 79 input were taken from a Gaussian distribution (Table 1).

**Table 1: Synaptic weights for intra-areal connections.** Mean synaptic weight  $\bar{w}$  and standard deviation  $\sigma_w$  for all possible synapses. E, I, and Input represent excitatory neurons, inhibitory neurons, and external input, respectively. The arrow indicates the direction of the connection.

Synapses	$\bar{w}$ (nS)	$\sigma_w$ (nS)
$E \rightarrow E$	2.5	1.0
$E \rightarrow I$	2.5	1.0
$I \rightarrow E$	240	10
$I \rightarrow I$	240	10
$Input \rightarrow E$	3.2	1.0
$Input \rightarrow I$	3.2	1.0

## 80 **2.3 Mouse large-scale cortical network**

81 The mouse cortex's large-scale network model comprises 19 cortical areas where a spiking neuronal  
82 population models each area with long-range and recurrent synapses. Parameters related to recurrent  
83 synapses were described in the previous session. Neurons from different areas are randomly  
84 connected with probability  $p_{\text{inter}} = 5\%$ . The synaptic weights between cortical areas are based  
85 on the recently published anatomical connectivity dataset for the mouse cortex [17] obtained by  
86 retrograde tracer injections [23]. This technique consists in injecting a tracer that flows from the  
87 target area to the cell bodies, allowing to identify neurons projecting to the target area. The Fraction  
88 of Labeled Neurons (FLN) was measured as the ratio of the number of labeled neurons in a source  
89 area to the total quantity of labeled neurons in all source areas [24, 25]. The synaptic weights for  
90 directed long-range connections are the FLNs scaled by the global scaling parameters  $\mu_E = 50$  and  
91  $\mu_I = 25$ ,

$$w_{\text{lr},E}^i = \mu_E \sum_j^N \text{FLN}_{i,j} \quad (13)$$

$$w_{\text{lr},I}^i = \mu_I \sum_j^N \text{FLN}_{i,j}. \quad (14)$$

92 Long-range connections as excitatory, targeting either excitatory or inhibitory neurons with synaptic  
93 weight,  $w_{\text{lr},E}^i$ , and  $w_{\text{lr},I}^i$ , respectively. The index  $j$  represents the source area,  $i$  the target area, and  $N$   
94 is the total number of simulated cortical areas. The axonal delay for long-range connections is given  
95 by the ratio between the anatomical distance estimates between cortical areas and the conduction  
96 speed set as 3.5 m/s [26].

## 97 **2.4 LFP signal**

98 We computed the local field potential (LFP) signal as a sum of the currents' absolute values acting  
99 upon excitatory neurons in a spiking neuronal population [27, 28]. Thus, for a cortical area in our

100 model, the LFP signal will be given by,

$$\text{LFP} = R \frac{\sum_i^{N_E} (|I_{E,i}| + |I_{I,i}| + |I_{\text{bkg},i}|)}{N_E}, \quad (15)$$

101  $I_{E,i}$  accounts for both the local (within population) and global (inter-areal projections) excitatory  
 102 synaptic currents, while  $I_{I,i}$  corresponds to the local inhibitory current.  $I_{\text{bkg},i}$  is the synaptic current  
 103 related to the background Poisson input.  $R$  represents the resistance of a typical electrode used for  
 104 extracellular measurements, here chosen to be 1 M $\Omega$  [19].  $N_E$  is the number of excitatory neurons  
 105 in each neuronal population.

106 The mean was subtracted from the simulated LFP signal. The resultant signal was filtered using a  
 107 low-pass filter in 1 kHz to avoid aliasing and downsampled to 1 kHz.

## 108 2.5 Generalized partial directed coherence

109 Generalized partial directed coherence (GPDC) is a frequency-domain method of directed functional  
 110 connectivity established on multivariate vector autoregressive (MVAR) model [29]. Considering  
 111 that LFP signals from all areas in the model are represented by a set  $\mathbf{x}(t) = [x_1(t) \cdots x_N(t)]^T$  of  
 112 simultaneously observed time series. The MVAR model for  $\mathbf{x}(t)$  is defined as:

$$\mathbf{x}(t) = \sum_{k=1}^p \mathbf{A}_k \mathbf{x}(t-k) + \epsilon(t) \quad (16)$$

113 where  $p$  is the MVAR model order.  $\mathbf{A}_k$  are coefficient matrices in which the element  $a_{ij}^{(k)}$  define the  
 114 effect of  $x_j(t-k)$  on  $x_i(t)$ . The term  $\epsilon(t)$  is a vector of  $N$  white noises with covariance matrix  $\Sigma$ .  
 115 The GPDC from the time series  $x_j$  to the time series  $x_i$  at frequency  $\lambda$  is defined as,

$$\text{GPDC}_{ij}(\lambda) = \left| \frac{\frac{1}{\sigma_i} \bar{A}_{ij}(\lambda)}{\sqrt{\sum_{k=1}^N \frac{1}{\sigma_k^2} \bar{A}_{kj}(\lambda) \bar{A}_{kj}^*(\lambda)}}} \right|^2, \quad (17)$$

116 where

$$\bar{A}_{ij}(\lambda) = \begin{cases} 1 - \sum_{k=1}^p A_{ij,k} e^{-2\pi\sqrt{-1}\lambda k}, & \text{if } i = j \\ - \sum_{k=1}^p A_{ij,k} e^{-2\pi\sqrt{-1}\lambda k}, & \text{if } i \neq j, \end{cases} \quad (18)$$

117 and  $\sigma_i^2$  refers to the variance of white noise  $\epsilon_i(t)$  [29].  $\lambda$  is a normalized frequency where  $\lambda = 0.5$   
 118 means one half of the sampling rate  $fs$  [30]. The MVAR model was estimated by the method of  
 119 ordinary least squares (OLS) [31]. Akaike's information criterion gave the model order indicated  
 120 that the best model order  $p$  that was lesser than or equal to 50 [30]. For all analysis it was evaluated  
 121 the peak of GPDC.

## 122 2.6 Weighted FLN and weighted GPDC

123 In order to investigate the propagation of neuronal activity through the links defined by structural  
 124 and directed functional connectivity, we defined the weighted FLN (wFLN) and the weighted GPDC  
 125 (wGPDC) [32],

$$\text{wFLN}_{ij} = \frac{1}{n} \sum_{j=1}^n \left( \frac{\text{FLN}_{ij} r_j}{\sum_{j \in S} r_j} \right) \quad (19)$$

$$\text{wGPDC}_{ij} = \frac{1}{n} \sum_{j=1}^n \left( \frac{\text{GPDC}_{ij} r_j}{\sum_{j \in S} r_j} \right) \quad (20)$$

126 where  $\text{FLN}_{ij}$  is the FLN from area  $j$  to area  $i$ ,  $r_j$  is the firing rate for area  $j$ ,  $\text{GPDC}_{ij}$  is the peak of  
 127 GPDC from area  $j$  to area  $i$ ,  $S$  is the set of source areas for target area  $i$  and finally  $n$  is the  
 128 cardinality of set  $S$ .

## 129 2.7 Numerical simulations

130 All simulations were performed using the simulator Brian2 [33] applying the exponential Euler  
 131 method [34] to integrate the differential equations with an integration step of 0.1 ms. Each simulating  
 132 was 30 s long, generating sufficient data points to apply GPDC on the simulated LFP signals [35].



### 133 3 Results

134 The model of the large-scale cortical network of the mouse is composed of 19 spiking neural  
 135 populations with recurrent connections and excitatory long-range connections constrained by the  
 136 directed and weighted structural connectome (Figure 1A and Figure 1B). The dynamical behavior of  
 137 each simulated cortical area is predominantly asynchronous with transient spike synchronization [36,  
 138 37] (Figure 1C). The power spectral density (PSD) of the LFP signal for a cortical area presents a  
 139 peak in the gamma band (Figure 1D and 1E) [38]. The firing rate of inhibitory neurons is  $4.74 \pm 0.11$ ,  
 140 higher than excitatory neurons rate of  $3.64 \pm 0.42$  (Figure 1F). Differences in population behavior are  
 141 mostly due to inputs from other areas since we sample their parameters from the same distributions  
 142 (Section 2.2).

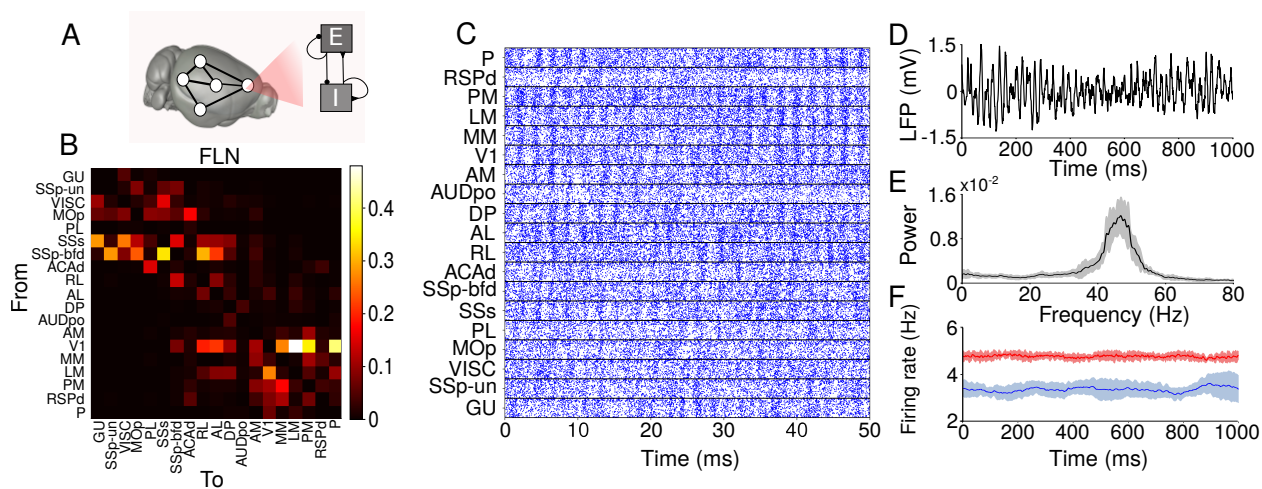


Figure 1: **Large-scale cortical network.** (A) Local neuronal population where E and I are populations of spiking neurons. (B) Map of structural connectivity given by the FLNs. These values define the strength of long-range projections in the large-scale network model. (C) Raster plot of 50ms of activity for each cortical area. (D) Simulated LFP signal for an area in the large-scale network model. (E) Power spectral density for simulated LFP signals from one area. Continuous black line corresponds to the average over ten simulations, and the gray shaded area delimits its standard deviation. (F) Firing-rate for excitatory (blue) and inhibitory (red) populations computed using a sliding window of 100ms. The continuous line corresponds to an average firing-rate over ten simulations, and the shaded area is the standard deviation. To exemplify, we used data from area MOp in (D), (E), and (F).

143 We first compared the FLN values to the average GPDC over ten simulations of the model. Many  
 144 medium to strong connections from the structural connectome were also captured by the directed

JANUARY 28, 2021

145 functional connectivity (Figure 2A and Figure 2B). We used the GPDC largest value (peak), but  
146 other approaches such as the average of GPDC over frequencies and area under the GPDC curve  
147 (Supplementary Figure S1) produced similar results.

148 Although the graph density of structural connectome is 97% [17], most structural connections are  
149 weak, which leads to a prevalence of weak average GPDC values. Weak structural connections are  
150 characteristics shared by connectomes from different mammals, with FLNs varying by several orders  
151 of magnitude, log-normally distributed [23, 39, 17, 40]. To evaluate the relation between structural  
152 and directed functional connectivity, we plotted GPDC values from ten simulations against FLNs  
153 and fit a linear model, obtaining the Pearson correlation  $r$  (Figure 2C). The scatter plot presents  
154 most points close to the origin due to the predominance of small values for the GPDC and FLN.  
155 Interestingly, for some FLNs, there is a high variation of GPDC values over different simulations.  
156 The Pearson correlation between FLN and GPDC is 0.73, and GPDC explains approximately 54%  
157 of the variance in FLN. This value similar to those obtained by other works that analyzed different  
158 structural connectomes using functional connectivity applied to empirical data [41, 42] or firing-rate  
159 models [43].

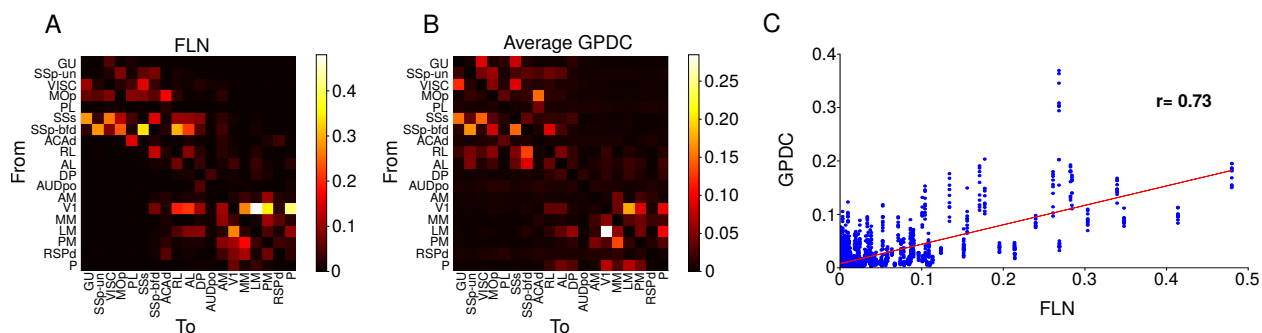


Figure 2: **Relation between structural and directed functional connectivity.** (A) Map of structural connectivity given by the FLNs. (B) Map of directed functional connectivity given by the average of GPDC peaks over ten simulations. (C) Scatter plot of FLNs *versus* GPDC peak. The red line corresponds to the linear fit. The Pearson correlation between FLNs and GPDC is 0.73.

160 We also investigated the propagation of activity between cortical areas through the pathways  
161 defined by structural and directed functional connectivity. The propagation of activity in the  
162 cortex is constrained by direct anatomical connections between areas and indirect paths [44], with

JANUARY 28, 2021

163 the propagation of activity occurring mainly through the strongest long-range projections [24].  
164 The weighted FLNs are strongly correlated to the target areas' firing rate (Figure 3A), while the  
165 correlation with the weighted GPDC and firing rate was 0.54 (Figure 3B). This indicates that neural  
166 activity propagation is directly dependent on the strength of structural connections and that GPDC  
167 can capture part of this activity propagation.

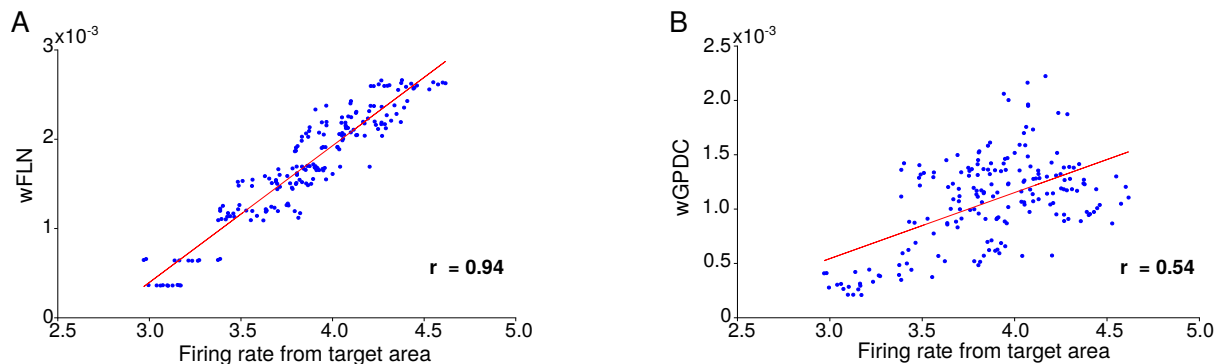


Figure 3: **Propagation of activity through structural and directed functional pathways.** (A) Weighted FLN *versus* the firing-rate for target areas. The Pearson correlation between Weighed FLNs and firing-rate for target areas is 0.94. (B) Weighted GPDC *versus* the firing-rate for target areas. The Pearson correlation between Weighed GPDC and firing-rate for target areas is 0.54. Red lines are linear fit.

168 We analyzed the behavior of GPDC estimates when considering a reduced number of areas, re-  
169 producing typical experimental setups. We considered a visual and a frontoparietal cluster, both  
170 composed of 7 cortical areas [17]. We evaluated the GPDC estimates between all areas of each  
171 cluster (Figures 4C and 4F), conditioned on the whole connectome (Figures 4B and 4E), conditioned  
172 on the areas in each cluster, and using only pairwise (bivariate) estimates (Figures 4D and 4G). This  
173 analysis simulates the situations where an electrophysiologist only has information from a single  
174 cluster of cortical areas or a pair of areas. The highest correlations between the GPDC and FLN  
175 occurred when we conditioned GPDC to the whole connectome, followed by GPDC conditioned to  
176 the cluster area, and pairwise GPDC. Also, in all cases, the correlation for the frontoparietal cluster  
177 was higher in all scenarios.

178 We extended the analysis to evaluate the effect of cluster size on GPDC correlation to FLN. We  
179 used cluster sizes ranging from 2 to 15 areas. We created 150 random clusters sampled from all

JANUARY 28, 2021

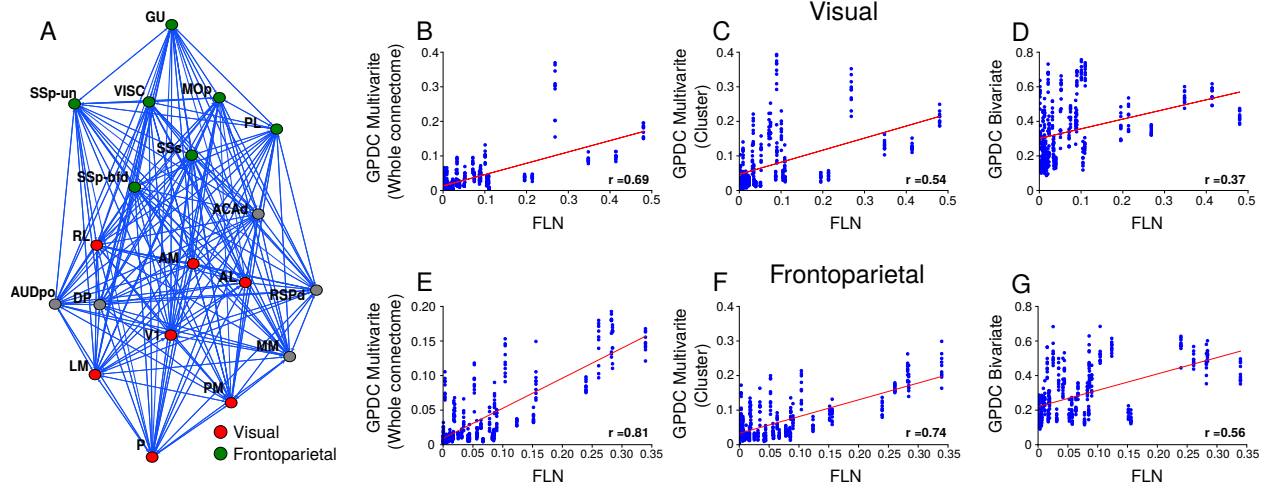


Figure 4: **Correlation between FLN and GPDC for the visual and frontoparietal clusters.** (A) Graph representing the mouse cortical connectome. Nodes represents cortical areas and edges, directed long-range projections between them. Green nodes are cortical areas belonging to the frontoparietal cluster. Red nodes are cortical areas belonging to the visual cluster. Both clusters are composed of 7 cortical areas. (B-D) FLN *versus* GPDC for the visual cluster. The GPDC was computed in (B) conditioned to the whole connectome, (C) conditioned to the areas in the cluster and (D) bivariate approach. (E-G) FLN *versus* GPDC for the frontoparietal cluster. The GPDC was computed in (E) conditioned to the whole connectome, (F) conditioned to the areas in the cluster and (G) bivariate approach. Red lines are linear fit and  $r$  is the Pearson correlation.

180 areas in the connectome for each cluster size and computed the Pearson correlation for (A) the  
181 GPDC conditioned on the whole connectome, (B) conditioned on the cluster areas, and (C) pairwise  
182 (bivariate). For cases (A) and (B), the Pearson correlation increases, and the standard variation  
183 decreases as we increase the cluster size (Figure 5A-B), showing that it is advantageous to include  
184 more areas in the GPDC calculation. Surprisingly, the results for scenarios A and B are similar,  
185 indicating that using signals measured in a few cortex areas is similar to using signals from the whole  
186 cortex, at least regarding the correlation between structural and directed functional connectivity.  
187 The correlation between whole connectome GPDC and cluster GPDC estimates increases for large  
188 clusters, as expected (Supplementary Figure S2). When considering the bivariate GPDC (Figure 5C),  
189 the average Pearson correlation decreases for a range of cluster sizes and remain stable in a low  
190 value, which shows that pairwise estimates of directed functional connectivity are affected by  
191 interference from ignored signals.

JANUARY 28, 2021

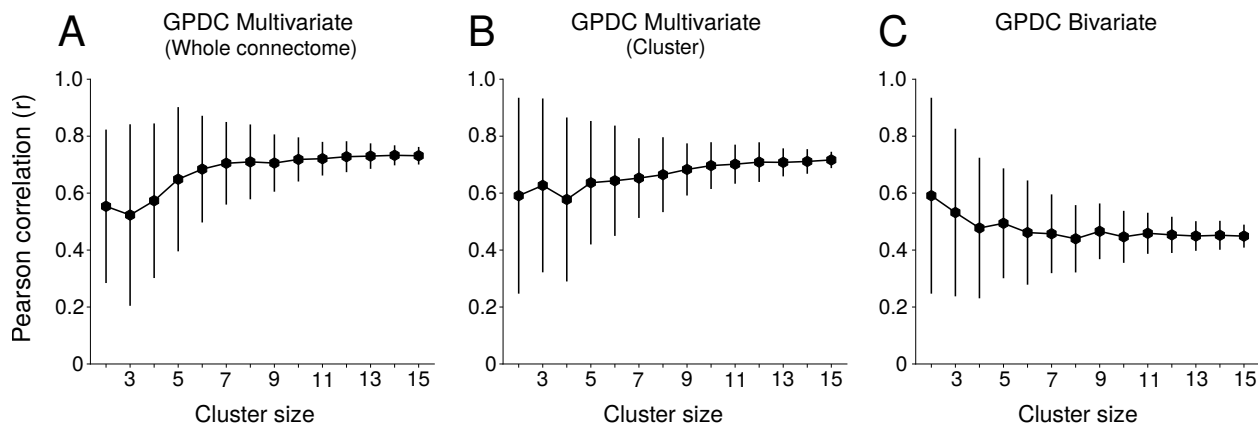


Figure 5: **Correlation between FLN and GPDC for the different cluster size with randomly chosen areas.** Average (black dots) and standard deviation (error bars) of Pearson correlation for different cluster size. (A) GPDC is conditioned to the whole connectome. (B) GPDC is conditioned only to areas in the cluster. (C) GPDC bivariate.

## 192 4 Discussion

193 We evaluated the inference of directed functional connectivity applying GPDC on simulated  
194 LFP signals generated from a large-scale network model for the mouse cortex. Our main result  
195 demonstrates that when GPDC is conditioned to a reduced number of areas or the whole connectome,  
196 the average Pearson correlation between structural and directed functional connectivity for both  
197 cases are comparable. This result provides evidence that it is possible to obtain a reliable relationship  
198 between structural and directed functional connectivity in electrophysiological experiments even  
199 when signals are recorded from few areas.

200 Pearson correlation between structural and directed functional connectivity considering the whole  
201 connectome and all possible connections in our model is in the range of values obtained in exper-  
202 imental works comparing structural connectivity obtained by tracers and (undirected) functional  
203 connectivity [45]. Specifically, previous studies comparing structural and functional connectivity in  
204 mice cortex obtained a lower Pearson correlation coefficient than ours [46, 47]. However, besides  
205 the undirected functional connectivity adopted in both studies, structural connectivity was set as  
206 undirected in one of them (long-range projection weights were given by the average of weights in 2

JANUARY 28, 2021

207 directions [46]). Also, recordings suffer the influence of the unrecorded source of activities what  
208 can affect the relationship between structural and functional connectivity [48].

209 Although large-scale network models have been used to investigate and predict brain activity  
210 observed in electrophysiology and neuroimage [24, 25, 49, 50], as far as we know, the relationship  
211 between structural and functional connectivity has been almost unexplored through large-scale  
212 network models [51]. Besides, most works in this subject used neural mass description (rate models)  
213 to describe each area's activity in the large-scale network model [52, 53]. However, the information  
214 propagated between brain regions can be characterized not only by the rate code but also by the  
215 temporal code [54, 55, 56, 57, 58]. Additionally, there are hypotheses pointing to spike-timing and  
216 spike coherence as essential components of cortical communication [59, 36, 60]. Thus, in our large-  
217 scale network model, a spiking neuronal population describes each cortical area's activity [24, 61].  
218 Although spiking neuronal populations are computationally expensive and sometimes prohibitive for  
219 large-scale network models simulating many connected brain areas, they present a rich possibility  
220 of dynamical behaviors that are not possible using rate models.

221 The structural connectivity obtained by tracer injections has the advantage that the FLNs between  
222 areas are not reciprocal [62], i.e., they are directional. Thus, the best approach to compare structural  
223 connectivity and functional connectivity was using a measure that provides the direction of influence  
224 from one signal to another. The mouse cortical connectome used in our large-scale network model  
225 was obtained through tracer injections [17]. For this reason, GPDC was a suitable choice for  
226 evaluating functional connectivity measures. GPDC is a frequency domain measure [29, 30].  
227 However, to have only one value representing the directed functional connectivity, we choose the  
228 peak of GPDC, which presented a better correlation with structural connectivity compared to other  
229 approaches (Figure S1).

230 In our results, although the GPDC peak is positively correlated with FLNs, there are several  
231 GPDC values that do not correspond to strong FLNs. There are some justifications for these  
232 mismatches between GPDC and FLNs. First, in some situations investigated using systems of

JANUARY 28, 2021

233 few neuronal populations, the direction and weight of directed functional connectivity estimates  
234 can be influenced by the phase relation between signals [36, 63, 64]. In large-scale network  
235 models, the system's heterogeneity, mainly due to axonal delays for long-range projections, can  
236 arise several phase differences between regions [65]. Thus, the relationship between structural  
237 and directed functional connectivity can be altered. Second, GPDC classifies the intensity of the  
238 connection regarding a signal source [30, 15], what is problematic for comparing with strength of  
239 structural connectivity [66]. Therefore, there might be cases where the functional coupling is strong  
240 concerning a particular source even though the synaptic projections are not.

241 The propagation of activity between simulated cortical areas is strongly correlated with weighted  
242 FLNs and moderately correlated with weighted GPDC estimates. There are several ways to  
243 analyze the propagation of activity in the cortex; some of them can be based only on structural  
244 connectivity [44], in amplification caused by changes in projections weights [24] and some based  
245 on alterations in firing rates [67]. However, to the best of our knowledge, no studies explore how  
246 to acquire signal propagation paths based on directed functional connectivity. Here, we based our  
247 analysis on the idea proposed by Cole et al. of activity flow [32]. As we verified in our results, the  
248 mean GPDC peak weighted by the firing rate from a source area is positively correlated to the target  
249 area's firing rate. Results are better when, instead of considering the GPDC peak, we considered the  
250 FLNs. This result suggests that signal propagation pathways are better determined by structural  
251 connectivity than by directed functional connectivity. The use of directed functional connectivity  
252 to infer signal propagation is not straightforward because several aspects of the model dynamics  
253 and some characteristics of the method applied can affect the inference of connections for directed  
254 functional connectivity.

255 The relationship between structural and directed functional connectivity is better when GPDC is  
256 conditioned to all areas in the connectome. However, when it is conditioned to few areas in a cluster,  
257 structural and directed functional connectivity are moderately correlated. Gămănut et al. identified  
258 6 cluster in the connectome (prefrontal, frontal, parietal, cingulate, temporal and visual) [17] based  
259 on the same approach used to investigate the macaque cortex [68]. We joined prefrontal, frontal

JANUARY 28, 2021

260 and parietal clusters in a single cluster called frontoparietal. The regions AUDpo, and DP, which  
261 compose the temporal cluster and ACAd, RSPd, and MM, which belong to the cingulate cluster  
262 were excluded from these calculations because they form clusters with small number of regions  
263 [17]. The idea was to evaluate the relationship between GPDC and FLNs in specific clusters with  
264 the same cluster size. The general results were the same for frontoparietal and visual clusters. For  
265 frontoparietal clusters, the range of values for FLN and GPDC is smaller than for visual cluster.  
266 The correlation between GPDC and FLN was better in the frontoparietal cluster, where even for the  
267 bivariate approach, GPDC and FLNs are moderately correlated.

268 The correlation between GPDC considering the whole connectome and GPDC considering the cluster  
269 increases with the number of areas considered in the measurement (Supplementary Figure S2A).  
270 Besides that, the difference between GPDC estimates for those two approaches decreases with  
271 the cluster size (Supplementary Figure S2B). It is well known that pairwise estimates of directed  
272 functional connectivity present false connections compared to structural connectivity, caused by  
273 common input or indirect connections [7, 14, 6]. Novelli et al. showed that the relation between  
274 structural and directed functional connectivity in a large-scale network model for the macaque brain  
275 is more accurate when the multivariate approach is applied to infer directed functional connectivity  
276 than for bivariate approach [52]. Nevertheless, it is uninvestigated the reliability of directed functional  
277 connectivity estimates according to the number of areas considered. With our results, we  
278 evaluated not only the relationship between structural and directed functional connectivity (Figure 4  
279 and Figure 5) for different cluster sizes but also the directed functional connectivity estimates when  
280 a reduced number of areas are considered (Figure S2).

281 Our large-scale network model has some limitations related to the similarity in different cortical  
282 areas' dynamical behavior and the connectome. First, modeled neuronal populations are practically  
283 homogeneous excepted by synaptic currents caused by long-range projections. However, in realistic  
284 approaches, several biologically based features can be added to the model, for example, cell types,  
285 spatial scales, and density of excitatory and inhibitory populations [69, 70, 71]. Second, still related  
286 to the homogeneity between cortical areas, the simulated LFP for areas in our large-scale network



JANUARY 28, 2021

287 model oscillates in gamma band (Figure 1). It is known that the activity of cortical areas in mice  
288 can oscillate in different bands [72, 73]. Also, oscillatory activity in the mouse cortex is related to  
289 density and type of inhibitory neurons [74, 75]. Recently, it has been shown that the relationship  
290 between structural and functional connectivity in the macaque cortex is frequency dependent [76].  
291 Third, it is shown that functional connectivity is dependent on network states [77]. Also, studies in  
292 computational neuroscience have been exploring multistability and temporal patterns of functional  
293 connectivity [78, 79, 80]. In our model, we did not explore network states and dynamics of directed  
294 functional connectivity. The computation of directed functional connectivity is dependent on the  
295 data length [35]. Thus, the evaluation of directed functional connectivity patterns in short windows  
296 of data can be untrustworthy because of the number of samples considered. Finally, we considered  
297 only cortical areas in our large-scale network model. It would be interesting to integrate subcortical  
298 areas into the model and verify their impact on the relationship between structural and functional  
299 connectivity. Future studies can overcome these limitations by creating more detailed models with  
300 biologically plausible neuronal features and connectome composed of cortical and subcortical  
301 areas [69, 81].

302 Our results shed light on the relationship between structural and directed functional connectivity in  
303 the circumstances near to those faced by electrophysiologists. We concluded that the reliability of  
304 directed functional connectivity estimates and the relationship with structural connectivity relies  
305 on the number of areas considered. Despite the limitations of our large-scale network model, our  
306 findings can support analysis based on electrophysiological recordings, and our model can be used  
307 for other investigations regarding cortical communication.

## 308 **References**

- 309 [1] Andrea Avena-Koenigsberger, Bratislav Misić, and Olaf Sporns. Communication dynamics in complex brain  
310 networks. *Nature Reviews Neuroscience*, 19(1):17, 2018.
- 311 [2] Karen S Ambrosen, Simon F Eskildsen, Max Hinne, Kristine Krug, Henrik Lundell, Mikkel N Schmidt, Marcel AJ  
312 van Gerven, Morten Mørup, and Tim B Dyrby. Validation of structural brain connectivity networks: The impact  
313 of scanning parameters. *NeuroImage*, 204:116207, 2020.
- 314 [3] Olaf Sporns, Giulio Tononi, and Rolf Kötter. The human connectome: a structural description of the human brain.  
315 *PLoS Comput Biol*, 1(4):e42, 2005.
- 316 [4] Danielle S Bassett, Perry Zurn, and Joshua I Gold. On the nature and use of models in network neuroscience.  
317 *Nature Reviews Neuroscience*, 19(9):566–578, 2018.
- 318 [5] Danielle S Bassett and Olaf Sporns. Network neuroscience. *Nature neuroscience*, 20(3):353–364, 2017.
- 319 [6] Andrew T Reid, Drew B Headley, Ravi D Mill, Ruben Sanchez-Romero, Lucina Q Uddin, Daniele Marinazzo,  
320 Daniel J Lurie, Pedro A Valdés-Sosa, Stephen José Hanson, Bharat B Biswal, et al. Advancing functional  
321 connectivity research from association to causation. *Nature neuroscience*, 22(11):1751–1760, 2019.
- 322 [7] André M Bastos and Jan-Mathijs Schoffelen. A tutorial review of functional connectivity analysis methods and  
323 their interpretational pitfalls. *Frontiers in systems neuroscience*, 9:175, 2016.
- 324 [8] Ronaldo V Nunes, Marcelo B Reyes, and Raphael Y De Camargo. Evaluation of connectivity estimates using  
325 spiking neuronal network models. *Biological cybernetics*, 113(3):309–320, 2019.
- 326 [9] Guosong Hong and Charles M Lieber. Novel electrode technologies for neural recordings. *Nature Reviews*  
327 *Neuroscience*, 20(6):330–345, 2019.
- 328 [10] Kenneth D Harris, Rodrigo Quiñan Quiroga, Jeremy Freeman, and Spencer L Smith. Improving data quality in  
329 neuronal population recordings. *Nature neuroscience*, 19(9):1165–1174, 2016.
- 330 [11] Marieke L Schölvinck, David A Leopold, Matthew J Brookes, and Patrick H Khader. The contribution of  
331 electrophysiology to functional connectivity mapping. *Neuroimage*, 80:297–306, 2013.
- 332 [12] Ruben Sanchez-Romero and Michael W Cole. Combining multiple functional connectivity methods to improve  
333 causal inferences. *Journal of Cognitive Neuroscience*, pages 1–15, 2019.
- 334 [13] Xichao Mi, Ning Cheng, and Tao Zhang. Performance comparison between gpdc and pcmi for measuring  
335 directionality of neural information flow. *Journal of Neuroscience Methods*, 227:57–64, 2014.

- 336 [14] Lionel Barnett and Anil K Seth. The mvgc multivariate granger causality toolbox: a new approach to granger-  
337 causal inference. *Journal of neuroscience methods*, 223:50–68, 2014.
- 338 [15] Luiz A Baccalá and Koichi Sameshima. Partial directed coherence: a new concept in neural structure determination.  
339 *Biological cybernetics*, 84(6):463–474, 2001.
- 340 [16] Leonardo Novelli, Patricia Wollstadt, Pedro Mediano, Michael Wibral, and Joseph T Lizier. Large-scale directed  
341 network inference with multivariate transfer entropy and hierarchical statistical testing. *Network Neuroscience*,  
342 3(3):827–847, 2019.
- 343 [17] Răzvan Gămănuț, Henry Kennedy, Zoltán Toroczka, Mária Ercsey-Ravasz, David C Van Essen, Kenneth  
344 Knoblauch, and Andreas Burkhalter. The mouse cortical connectome, characterized by an ultra-dense cortical  
345 graph, maintains specificity by distinct connectivity profiles. *Neuron*, 97(3):698–715, 2018.
- 346 [18] Yoram Gutfreund, I Segev, et al. Subthreshold oscillations and resonant frequency in guinea-pig cortical neurons:  
347 physiology and modelling. *The Journal of physiology*, 483(3):621–640, 1995.
- 348 [19] Belén Sancristóbal, Raul Vicente, and Jordi Garcia-Ojalvo. Role of frequency mismatch in neuronal communica-  
349 tion through coherence. *Journal of computational neuroscience*, 37(2):193–208, 2014.
- 350 [20] Alessandro Barardi, Belen Sancristóbal, and Jordi Garcia-Ojalvo. Phase-coherence transitions and communication  
351 in the gamma range between delay-coupled neuronal populations. *PLoS computational biology*, 10(7):e1003723,  
352 2014.
- 353 [21] Belén De Sancristóbal, Raul Vicente, Jose Maria Sancho, and Jordi Garcia-Ojalvo. Emergent bimodal firing  
354 patterns implement different encoding strategies during gamma-band oscillations. *Frontiers in computational*  
355 *neuroscience*, 7:18, 2013.
- 356 [22] Petar Tomov, Rodrigo FO Pena, Michael A Zaks, and Antonio C Roque. Sustained oscillations, irregular firing,  
357 and chaotic dynamics in hierarchical modular networks with mixtures of electrophysiological cell types. *Frontiers*  
358 *in computational neuroscience*, 8:103, 2014.
- 359 [23] Nikola T Markov, MM Ercsey-Ravasz, AR Ribeiro Gomes, Camille Lamy, Loic Magrou, Julien Vezoli, P Misery,  
360 A Falchier, R Quilodran, MA Gariel, et al. A weighted and directed interareal connectivity matrix for macaque  
361 cerebral cortex. *Cerebral cortex*, 24(1):17–36, 2014.
- 362 [24] Madhura R Joglekar, Jorge F Mejias, Guangyu Robert Yang, and Xiao-Jing Wang. Inter-areal balanced amplifica-  
363 tion enhances signal propagation in a large-scale circuit model of the primate cortex. *Neuron*, 98(1):222–234,  
364 2018.

- 365 [25] Jorge F Mejias, John D Murray, Henry Kennedy, and Xiao-Jing Wang. Feedforward and feedback frequency-  
366 dependent interactions in a large-scale laminar network of the primate cortex. *Science advances*, 2(11):e1601335,  
367 2016.
- 368 [26] Hannah Choi and Stefan Mihalas. Synchronization dependent on spatial structures of a mesoscopic whole-brain  
369 network. *PLoS computational biology*, 15(4):e1006978, 2019.
- 370 [27] Alberto Mazzoni, Henrik Linden, Hermann Cuntz, Anders Lansner, Stefano Panzeri, and Gaute T Einevoll.  
371 Computing the local field potential (lfp) from integrate-and-fire network models. *PLoS computational biology*,  
372 11(12), 2015.
- 373 [28] Alberto Mazzoni, Stefano Panzeri, Nikos K Logothetis, and Nicolas Brunel. Encoding of naturalistic stimuli by  
374 local field potential spectra in networks of excitatory and inhibitory neurons. *PLoS Comput Biol*, 4(12):e1000239,  
375 2008.
- 376 [29] Luiz A Baccala, K Sameshima, and DY Takahashi. Generalized partial directed coherence. In *2007 15th*  
377 *International conference on digital signal processing*, pages 163–166. IEEE, 2007.
- 378 [30] Koichi Sameshima and Luiz Antonio Baccala. *Methods in brain connectivity inference through multivariate time*  
379 *series analysis*. CRC press, 2014.
- 380 [31] JD Hamilton. Times series analysis, one of princeton university press’s notable centenary titles. *Hard over*, 1994.
- 381 [32] Michael W Cole, Takuya Ito, Danielle S Bassett, and Douglas H Schultz. Activity flow over resting-state networks  
382 shapes cognitive task activations. *Nature neuroscience*, 19(12):1718–1726, 2016.
- 383 [33] Marcel Stimberg, Romain Brette, and Dan FM Goodman. Brian 2, an intuitive and efficient neural simulator.  
384 *Elife*, 8:e47314, 2019.
- 385 [34] James M Bower and David Beeman. *The book of GENESIS: exploring realistic neural models with the GEneral*  
386 *NEural Simulation System*. Springer Science & Business Media, 2012.
- 387 [35] Sara Sommariva, Alberto Sorrentino, Michele Piana, Vittorio Pizzella, and Laura Marzetti. A comparative study of  
388 the robustness of frequency-domain connectivity measures to finite data length. *Brain topography*, 32(4):675–695,  
389 2019.
- 390 [36] Agostina Palmigiano, Theo Geisel, Fred Wolf, and Demian Battaglia. Flexible information routing by transient  
391 synchrony. *Nature neuroscience*, 20(7):1014, 2017.
- 392 [37] Peter Uhlhaas, Gordon Pipa, Bruss Lima, Lucia Melloni, Sergio Neuenschwander, Danko Nikolić, and Wolf  
393 Singer. Neural synchrony in cortical networks: history, concept and current status. *Frontiers in integrative*  
394 *neuroscience*, 3:17, 2009.

JANUARY 28, 2021

- 395 [38] György Buzsáki and Xiao-Jing Wang. Mechanisms of gamma oscillations. *Annual review of neuroscience*,  
396 35:203–225, 2012.
- 397 [39] Panagiota Theodoni, Piotr Majka, David H Reser, Daniel K Wójcik, Marcello GP Rosa, and Xiao-Jing Wang.  
398 Structural attributes and principles of the neocortical connectome in the marmoset monkey. *bioRxiv*, 2020.
- 399 [40] György Buzsáki and Kenji Mizuseki. The log-dynamic brain: how skewed distributions affect network operations.  
400 *Nature Reviews Neuroscience*, 15(4):264–278, 2014.
- 401 [41] Patric Hagmann, Leila Cammoun, Xavier Gigandet, Reto Meuli, Christopher J Honey, Van J Wedeen, and Olaf  
402 Sporns. Mapping the structural core of human cerebral cortex. *PLoS Biol*, 6(7):e159, 2008.
- 403 [42] Maxwell H Turner, Kevin Mann, and Thomas R Clandinin. The connectome predicts resting state functional  
404 connectivity across the drosophila brain. *bioRxiv*, 2020.
- 405 [43] Rishidev Chaudhuri, Kenneth Knoblauch, Marie-Alice Gariel, Henry Kennedy, and Xiao-Jing Wang. A large-scale  
406 circuit mechanism for hierarchical dynamical processing in the primate cortex. *Neuron*, 88(2):419–431, 2015.
- 407 [44] Bertha Vézquez-Rodríguez, Zhen-Qi Liu, Patric Hagmann, and Bratislav Misic. Signal propagation via cortical  
408 hierarchies. *Network Neuroscience*, 4(4):1072–1090, 2020.
- 409 [45] Milou Straathof, Michel RT Sinke, Rick M Dijkhuizen, and Willem M Otte. A systematic review on the  
410 quantitative relationship between structural and functional network connectivity strength in mammalian brains.  
411 *Journal of Cerebral Blood Flow & Metabolism*, 39(2):189–209, 2019.
- 412 [46] James M Stafford, Benjamin R Jarrett, Oscar Miranda-Dominguez, Brian D Mills, Nicholas Cain, Stefan  
413 Mihalas, Gareth P Lahvis, K Matthew Lattal, Suzanne H Mitchell, Stephen V David, et al. Large-scale topology  
414 and the default mode network in the mouse connectome. *Proceedings of the National Academy of Sciences*,  
415 111(52):18745–18750, 2014.
- 416 [47] Joanes Grandjean, Valerio Zerbi, Joshua Henk Balsters, Nicole Wenderoth, and Markus Rudin. Structural basis of  
417 large-scale functional connectivity in the mouse. *Journal of Neuroscience*, 37(34):8092–8101, 2017.
- 418 [48] Shuixia Guo, Anil K Seth, Keith M Kendrick, Cong Zhou, and Jianfeng Feng. Partial granger causal-  
419 ity—eliminating exogenous inputs and latent variables. *Journal of neuroscience methods*, 172(1):79–93, 2008.
- 420 [49] Murat Demirtaş, Carles Falcon, Alan Tucholka, Juan Domingo Gispert, José Luis Molinuevo, and Gustavo Deco.  
421 A whole-brain computational modeling approach to explain the alterations in resting-state functional connectivity  
422 during progression of alzheimer’s disease. *NeuroImage: Clinical*, 16:343–354, 2017.
- 423 [50] Michael Breakspear. Dynamic models of large-scale brain activity. *Nature neuroscience*, 20(3):340–352, 2017.

- 424 [51] Kanika Bansal, Johan Nakuci, and Sarah Feldt Muldoon. Personalized brain network models for assessing  
425 structure–function relationships. *Current Opinion in Neurobiology*, 52:42–47, 2018.
- 426 [52] Leonardo Novelli and Joseph T Lizier. Inferring network properties from time series using transfer entropy  
427 and mutual information: validation of multivariate versus bivariate approaches. *Network Neuroscience*, (Just  
428 Accepted):1–52, 2020.
- 429 [53] Christopher J Honey, Olaf Sporns, Leila Cammoun, Xavier Gigandet, Jean-Philippe Thiran, Reto Meuli, and  
430 Patric Hagmann. Predicting human resting-state functional connectivity from structural connectivity. *Proceedings  
431 of the National Academy of Sciences*, 106(6):2035–2040, 2009.
- 432 [54] Malte Bieler, Kay Sieben, Nicole Cichon, Sandra Schildt, Brigitte Röder, and Ileana L Hanganu-Opatz. Rate and  
433 temporal coding convey multisensory information in primary sensory cortices. *eneuro*, 4(2), 2017.
- 434 [55] Anil K Seth. Neural coding: rate and time codes work together. *Current Biology*, 25(3):R110–R113, 2015.
- 435 [56] Gerald Hahn, Adrian Ponce-Alvarez, Gustavo Deco, Ad Aertsen, and Arvind Kumar. Portraits of communication  
436 in neuronal networks. *Nature Reviews Neuroscience*, 20(2):117–127, 2019.
- 437 [57] Arvind Kumar, Stefan Rotter, and Ad Aertsen. Spiking activity propagation in neuronal networks: reconciling  
438 different perspectives on neural coding. *Nature reviews neuroscience*, 11(9):615–627, 2010.
- 439 [58] Artur Luczak, Bruce L McNaughton, and Kenneth D Harris. Packet-based communication in the cortex. *Nature  
440 Reviews Neuroscience*, 16(12):745–755, 2015.
- 441 [59] Gerald Hahn, Alejandro F Bujan, Yves Frégnac, Ad Aertsen, and Arvind Kumar. Communication through  
442 resonance in spiking neuronal networks. *PLoS computational biology*, 10(8):e1003811, 2014.
- 443 [60] Paul HE Tiesinga and Terrence J Sejnowski. Mechanisms for phase shifting in cortical networks and their role in  
444 communication through coherence. *Frontiers in human neuroscience*, 4:196, 2010.
- 445 [61] Maximilian Schmidt, Rembrandt Bakker, Kelly Shen, Gleb Bezgin, Markus Diesmann, and Sacha Jennifer van  
446 Albada. A multi-scale layer-resolved spiking network model of resting-state dynamics in macaque visual cortical  
447 areas. *PLoS computational biology*, 14(10):e1006359, 2018.
- 448 [62] Xiao-Jing Wang, Ulises Pereira, Marcello GP Rosa, and Henry Kennedy. Brain connectomes come of age. *Current  
449 Opinion in Neurobiology*, 65:152–161, 2020.
- 450 [63] Fernanda S Matias, Leonardo L Gollo, Pedro V Carelli, Steven L Bressler, Mauro Copelli, and Claudio R Mirasso.  
451 Modeling positive granger causality and negative phase lag between cortical areas. *NeuroImage*, 99:411–418,  
452 2014.

- 453 [64] Vasily A Vakorin, Bratislav Mišić, Olga Krakovska, Gleb Bezgin, and Anthony R McIntosh. Confounding effects  
454 of phase delays on causality estimation. *PLOS one*, 8(1):e53588, 2013.
- 455 [65] Spase Petkoski, J Matias Palva, and Viktor K Jirsa. Phase-lags in large scale brain synchronization: Methodological  
456 considerations and in-silico analysis. *PLoS computational biology*, 14(7):e1006160, 2018.
- 457 [66] Björn Schelter, Jens Timmer, and Michael Eichler. Assessing the strength of directed influences among neural  
458 signals using renormalized partial directed coherence. *Journal of neuroscience methods*, 179(1):121–130, 2009.
- 459 [67] Navid Hasanzadeh, Mohammadreza Rezaei, Sayan Faraz, Milos R Popovic, and Milad Lankarany. Necessary  
460 conditions for reliable propagation of slowly time-varying firing rate. *Frontiers in computational neuroscience*,  
461 14:64, 2020.
- 462 [68] Mária Ercsey-Ravasz, Nikola T Markov, Camille Lamy, David C Van Essen, Kenneth Knoblauch, Zoltán Toroczkai,  
463 and Henry Kennedy. A predictive network model of cerebral cortical connectivity based on a distance rule. *Neuron*,  
464 80(1):184–197, 2013.
- 465 [69] Csaba Erő, Marc-Oliver Gewaltig, Daniel Keller, and Henry Markram. A cell atlas for the mouse brain. *Frontiers*  
466 *in neuroinformatics*, 12:84, 2018.
- 467 [70] Quanxin Wang, Song-Lin Ding, Yang Li, Josh Royall, David Feng, Phil Lesnar, Nile Graddis, Maitham Naemi,  
468 Benjamin Facer, Anh Ho, et al. The allen mouse brain common coordinate framework: A 3d reference atlas. *Cell*,  
469 2020.
- 470 [71] Daniel Keller, Csaba Erő, and Henry Markram. Cell densities in the mouse brain: a systematic review. *Frontiers*  
471 *in neuroanatomy*, 12:83, 2018.
- 472 [72] Tomokazu Tsurugizawa, Boucif Djemai, and Andrew Zalesky. The impact of fasting on resting state brain  
473 networks in mice. *Scientific reports*, 9(1):1–12, 2019.
- 474 [73] Maxwell A Sherman, Shane Lee, Robert Law, Saskia Haegens, Catherine A Thorn, Matti S Hämäläinen,  
475 Christopher I Moore, and Stephanie R Jones. Neural mechanisms of transient neocortical beta rhythms: Converging  
476 evidence from humans, computational modeling, monkeys, and mice. *Proceedings of the National Academy of*  
477 *Sciences*, 113(33):E4885–E4894, 2016.
- 478 [74] Katerina Kalemaki, Xanthippi Konstantoudaki, Simona Tivodar, Kyriaki Sidiropoulou, and Domna Karagogeos.  
479 Mice with decreased number of interneurons exhibit aberrant spontaneous and oscillatory activity in the cortex.  
480 *Frontiers in neural circuits*, 12:96, 2018.

JANUARY 28, 2021

- 481 [75] Guang Chen, Yuan Zhang, Xiang Li, Xiaochen Zhao, Qian Ye, Yingxi Lin, Huizhong W Tao, Malte J Rasch,  
482 and Xiaohui Zhang. Distinct inhibitory circuits orchestrate cortical beta and gamma band oscillations. *Neuron*,  
483 96(6):1403–1418, 2017.
- 484 [76] Julien Vezoli, Martin Vinck, Conrado Arturo Bosman, André Moraes Bastos, Christopher Murphy Lewis, Henry  
485 Kennedy, and Pascal Fries. The role of anatomical connection strength for interareal communication in macaque  
486 cortex. *Available at SSRN 3751057*, 2020.
- 487 [77] Iain Stitt, Karl J Hollensteiner, Edgar Galindo-Leon, Florian Pieper, Eva Fiedler, Thomas Stieglitz, Gerhard  
488 Engler, Guido Nolte, and Andreas K Engel. Dynamic reconfiguration of cortical functional connectivity across  
489 brain states. *Scientific reports*, 7(1):1–14, 2017.
- 490 [78] Mathieu Golos, Viktor Jirsa, and Emmanuel Dauce. Multistability in large scale models of brain activity. *PLoS*  
491 *computational biology*, 11(12):e1004644, 2015.
- 492 [79] Patricio Orio, Marilyn Gatica, Rubén Herzog, Jean Paul Maidana, Samy Castro, and Kesheng Xu. Chaos versus  
493 noise as drivers of multistability in neural networks. *Chaos: An Interdisciplinary Journal of Nonlinear Science*,  
494 28(10):106321, 2018.
- 495 [80] Gustavo Deco and Viktor K Jirsa. Ongoing cortical activity at rest: criticality, multistability, and ghost attractors.  
496 *Journal of Neuroscience*, 32(10):3366–3375, 2012.
- 497 [81] Joseph E Knox, Kameron Decker Harris, Nile Graddis, Jennifer D Whitesell, Hongkui Zeng, Julie A Harris,  
498 Eric Shea-Brown, and Stefan Mihalas. High-resolution data-driven model of the mouse connectome. *Network*  
499 *Neuroscience*, 3(1):217–236, 2018.



# Supplementary Material

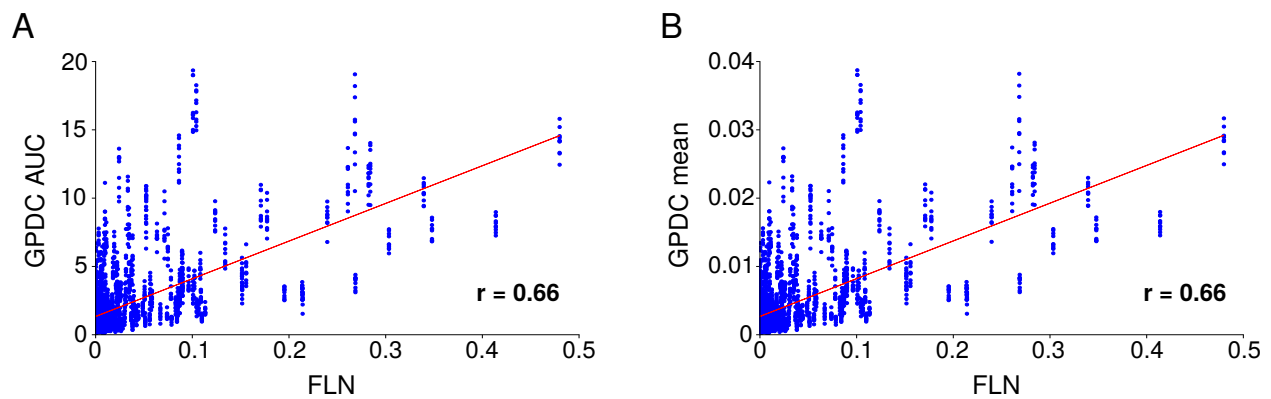
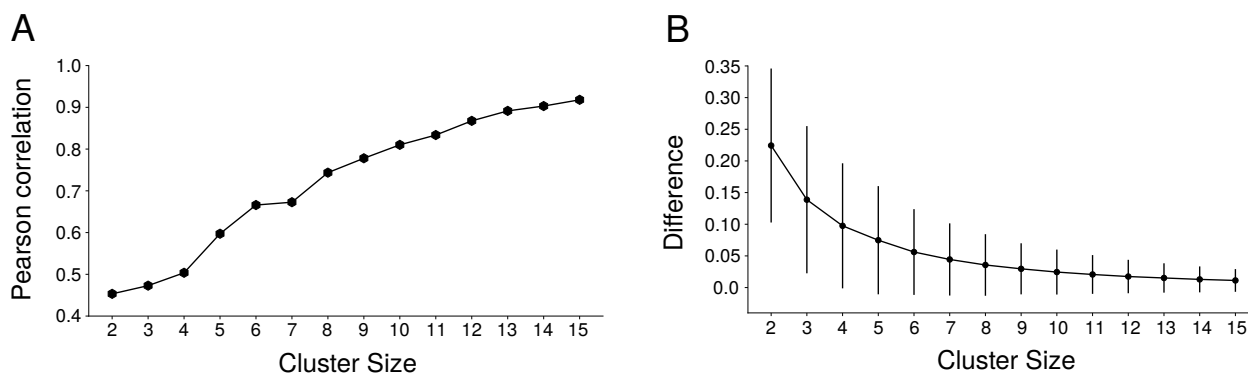


Figure S1: **Area Under Curve (AUC) and mean of GPDC estimates** . (A) GPDC AUC *versus* FLN. (B) GPDC mean *versus* FLN. In both cases, the Pearson correlation between GPDC mean or AUC and FLN is 0.66. Red lines are linear fit.

JANUARY 28, 2021



**Figure S2: Correlation and difference between GPDC estimates conditioned to the whole connectome and GPDC estimates conditioned to the cluster areas.** A) Pearson correlation increases with the cluster size. Each bullet represents the average Pearson correlation over 150 clusters composed of randomly chosen areas. Comparing all cluster sizes, the highest value for standard deviation of Pearson correlation is 0.07. B) Average difference between GPDC estimates conditioned to the whole connectome and GPDC estimates conditioned to the cluster areas. Average and standard deviation decrease with the cluster size.

Table S1: **Name of areas in mouse cortical connectome.** Adapted from Gămănut et. al., 2018.

<b>Abbreviations</b>	<b>Areas</b>
ACAd	Anterior cingulate area dorsal part
AL	Anterolateral area
AM	Anteromedial area
AUDpo	Auditory cortex posterior area
DP	Dorsal posterior area
GU	Gustatory area
LM	Lateromedial area
MM	Mediomedial area
MOp	Motor cortex primary
P	Posterior area
PL	Prelimbic area
PM	Posteromedial area
RL	Rostrolateral area
RSPd	Rostroplenia area dorsal part
SSp-bfd	Somatosensory cortex primary barrel field
SSp-un	Somatosensory cortex primary unassigned
SSs	Somatosensory cortex secondary
V1	Primary visual area
VISC	Visceral area